

Kinematics of RR Lyrae stars in the Galactic bulge with OGLE-IV and Gaia DR2

Hangci Du,¹★ Shude Mao,^{1,2} E. Athanassoula,³

Juntai Shen,^{4,5,6,7} and Pawel Pietrukowicz⁸

¹Department of Astronomy and Tsinghua Center for Astrophysics, Tsinghua University, 100084 Beijing, China

²National Astronomical Observatories, Chinese Academy of Sciences, 20A Datun Road, Chaoyang District, Beijing 100101, China

³Aix Marseille Université, CNRS, CNES, LAM, Marseille, 13388 Marseille Cedex 13, France

⁴Department of Astronomy, School of Physics and Astronomy, Shanghai Jiao Tong University, 800 Dongchuan Road, Shanghai 200240, China;

⁵Shanghai Key Laboratory for Particle Physics and Cosmology, 200240, Shanghai, China

⁶Shanghai Astronomical Observatory, Chinese Academy of Sciences, 80 Nandan Road, Shanghai 200030, China

⁷College of Astronomy and Space Sciences, University of Chinese Academy of Sciences, 19A Yuquan Road, Beijing 100049, China

⁸Astronomical Observatory, University of Warsaw, Al. Ujazdowskie 4, 00-478 Warszawa, Poland

Accepted 2020 August 24. Received August 21; in original form 2020 March 16

ABSTRACT

We analyze the kinematics and spatial distribution of 15,599 fundamental-mode RR Lyrae (RRL) stars in the Milky Way bulge by combining OGLE-IV photometric data and Gaia DR2 proper motions. We show that the longitudinal proper motions and the line-of-sight velocities can give similar results for the rotation in the Galactic central regions. The angular velocity of bulge RRLs is found to be around $35 \text{ km s}^{-1} \text{ kpc}^{-1}$, significantly smaller than that for the majority of bulge stars ($50 - 60 \text{ km s}^{-1} \text{ kpc}^{-1}$); bulge RRLs have larger velocity dispersion ($120 - 140 \text{ km s}^{-1}$) than younger stars. The dependence of the kinematics of the bulge RRLs on their metallicities is shown by their rotation curves and spatial distributions. Metal-poor RRLs ($[\text{Fe}/\text{H}] < -1$) show a smaller bar angle than metal-rich ones. We also find clues suggesting that RRLs in the bulge are not dominated by halo stars. These results might explain some previous conflicting results over bulge RRLs and help understand the chemodynamical evolution of the Galactic bulge.

Key words: Galaxy: bulge – Galaxy: kinematics and dynamics – Galaxy: structure

1 INTRODUCTION

RR Lyraes (RRL, hereafter) are pulsating, low-metallicity, core-helium-burning horizontal branch giants with age > 11 Gyr (Walker 1989) and trace an old, relatively metal-poor population in the bulge (Barbuy et al. 2018). They are standard candles for distance determination using the period-luminosity relation. These properties make RRL population an important tracer to study the bulge dynamics and evolution, even though they are estimated to represent only 1% of the Galactic bulge population (Pietrukowicz et al. 2012; Nataf et al. 2013).

There have been several disputes over the properties of RRLs in the Galactic bulge¹. In terms of the structure of RR Lyraes, Dékány et al. (2013) argued that bulge RRLs, with a bar angle of $12^\circ.5 \pm 0^\circ.5$, do not trace the standard bar structure (bar angle $\sim 27^\circ$, Wegg & Gerhard 2013); Gran et al. (2016) concluded that RRLs in high Galactic latitude ($-10.3^\circ \lesssim b \lesssim -8.0^\circ$) show no evidence of an X-

shaped structure, which also supports the postulate that RR Lyraes do not follow the bar structure; Pietrukowicz et al. (2015) analyzed the bulge RRL sample from the OGLE-IV survey (Soszyński et al. 2014) and concluded that the bar angle is $\sim 21^\circ$, considerably larger than that from Dékány et al. (2013), they also presented that the RRLs show evidence of a triaxial distribution. In terms of the origin of RR Lyraes, Dékány et al. (2018) proposed that bulge RRLs might correspond to the outskirts of an ancient Galactic spheroid or classical bulge component residing in the Galactic centre, while Mateu & Vivas (2018) favoured a thick disc with short scale height and short scale length. In terms of the kinematics of RR Lyraes, Wegg et al. (2019) showed that the rotation of RRLs at a distance of 1.5 kpc from the Galactic centre is $\sim 50 \text{ km s}^{-1}$, which, as he said, is in disagreement with the model by Pérez-Villegas et al. (2017).

Line-of-sight (LOS, hereafter) velocity and proper motion are two kinds of fundamental kinematics observables, both of which can be used to generate rotation curves in the Galactic bulge (e.g., Nataf et al. 2013; Clarkson et al. 2018); our paper will connect these two kinds of rotation curves. Due to the technical progress in massive spectroscopic observations, there have been many LOS

★ E-mail: hangci.du@outlook.com

¹ sometimes referred to as the "inner Galaxy" in the literature

velocity surveys probing stars toward the Galactic bulge in the past ten years: BRAVA (Howard et al. 2008; Kunder et al. 2012), ARGOS (Freeman et al. 2013; Ness et al. 2013), GIBS (Zoccali et al. 2017), GES (Rojas-Arriagada et al. 2014), APOGEE (Zasowski et al. 2016; Ness et al. 2016). In contrast, proper motion (PM) surveys are much less. HST SWEEPS survey (Clarkson et al. 2008, 2018) tried to use proper motions as bulge rotation indicators. However, it only gave a qualitative but not quantitative description due to their large distance uncertainty. In our work, we will demonstrate the equivalence of the proper motion and the line-of-sight velocity as bulge rotation indicators. Thanks to Gaia DR2 (Gaia Collaboration et al. 2016, 2018) with proper motions and OGLE-IV RR Lyrae sample (Pietrukowicz et al. 2015) with distance, we can study bulge kinematics using proper motions. Wegg et al. (2019) have dealt with PanSTARRS1 halo RRLs 1.5 – 20 kpc from the Galactic centre, while our work concentrates on RRLs in the innermost 1.5 kpc from the Galactic centre.

A further aim of this paper is to use RRL stars to probe the metallicity-kinematics correlation in the bulge region and the bulge formation history. Several surveys have studied the kinematics of other types of bulge stars with different metallicities. Within a radius of 3.5 kpc around the Galactic centre, Ness et al. (2013) found different kinematics in four metallicity bins, among which the stars with $[\text{Fe}/\text{H}] > -0.5$ show a near-cylindrical, faster rotation, while the stars with $[\text{Fe}/\text{H}] < -0.5$ have a significantly slower rotation, which is consistent with Ness et al. (2016) results combining APOGEE and ARGOS data. GIBS (Zoccali et al. 2017) divides their targeting red clumps and red-giant-branch stars in the inner bulge ($|l| \leq 8.5^\circ$, $b = 1.4 - 8.5^\circ$) into two groups separated approximately at $[\text{Fe}/\text{H}] = 0$, showing that the metal-poor component has a higher radial velocity dispersion compared to the metal-rich one at all longitudes. GES (Rojas-Arriagada et al. 2014, 2017) gave similar results as GIBS. HST SWEEPS (Clarkson et al. 2018) also found an evident trend that metal-poor bulge stars rotate slower than metal-rich ones. A slower rotation curve was also found for the metal-poor stars in PIGS (Arentsen et al. 2020). This phenomenon also appears in our work.

The paper is organized as follows: In section 2, we briefly introduce the sample we use. In section 3, we derive the relationship of PM and LOS velocities as bulge rotation indicators geometrically and validate it with mock data. In section 4, we show several results from the RRL distribution in spatial and velocity space and compare them with results from other surveys. In section 5, we explain why previous surveys on RRLs in the Galactic bulge did not observe the rotation quantitatively. We summarize and conclude in section 6.

2 DATA

The original sample of our work is from Soszyński et al. (2014); Udalski et al. (2015), which got an update by Soszyński et al. (2019). The sample consists of 38,257 RRLs over 182 square degrees (see Soszyński et al. 2014, their Figure 2 for the coverage on the sky), within which 27,258 are high-amplitude fundamental-mode RRab type stars. The photometry of the catalog was based on the Cousins I-band with 100 s exposure (ranging from about 13 mag to 20.5 mag). The Johnson V-band with 150 s exposure was also added for color information. RRLs were identified by Fourier analyses of the light curves. Metallicities were obtained from the Fourier coefficients. The completeness of the RRab stars in the sample is estimated to be 96% ~ 97% (Soszyński et al. 2014, 2019), which means we can safely obtain the star-count map and the spatial number density.

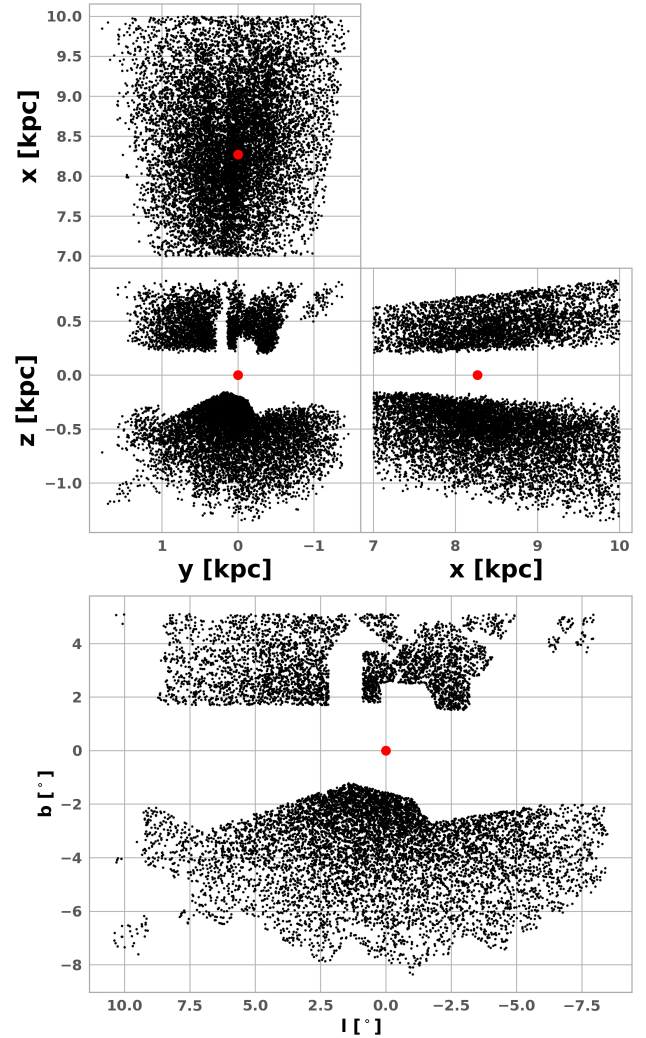


Figure 1. Face-on and side-on distribution of the OGLExGaia sample in Cartesian coordinate system; red dots are the Galactic center. Our whole sample covers 0 ~ 20 kpc in the x-direction, while we only show the inner 3 kpc for better visualization. For consistency, we use here the distance to the Galactic centre (GC) of 8.27 kpc (Pietrukowicz et al. 2015).

We follow the cleaning process by Pietrukowicz et al. (2015) as follows: we first take the sample of 27,258 RRab variables and reject 54 stars as being bona fide members and very likely members of eight globular clusters. Second, the sample was cleaned from the foreground and background RR Lyrae stars by constructing the color-magnitude ($V-I$, I) diagram (Pietrukowicz et al. 2015, their Figure 1), leading to a sample of 21,026 objects. It was also based on the color-magnitude diagram that the sample of RRab stars is complete down to $I=18$ mag. Finally, the region with a mean brightness of $I > 18$ mag (Pietrukowicz et al. 2015, their Figure 2) is excluded, leaving with only the "complete" area with all RRab stars presumed to be detected, which amounts to 16221 objects in 90.5 deg^2 .

The distance of the RRab stars is determined according to Pietrukowicz et al. (2015):

$$d = 10^{1+0.2(I_0-M_I)} = 10^{1+0.2(I-A_I-M_I)}, \quad (1)$$

where A_I was derived from the formula introduced in Nataf et al.

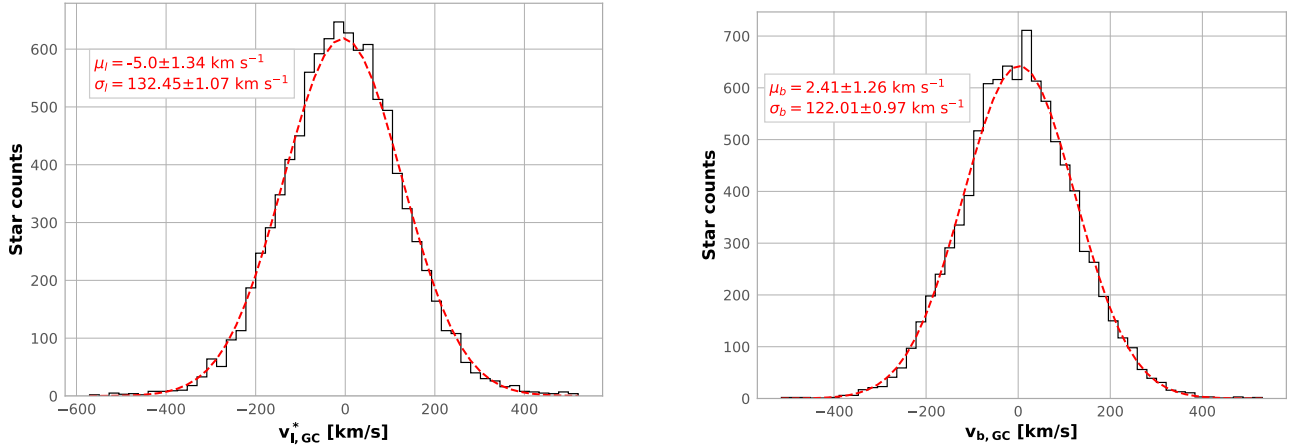


Figure 2. The transverse velocity distributions derived from proper motions of OGLExGaia RRLs in l and b . The best Gaussian fit is shown as the dashed curve; the mean and dispersion are indicated in each panel. We can see $\langle v_b \rangle \sim 0$, dispersion ratio $\sigma_l/\sigma_b \sim 1.1$; both are consistent with previous results (Reid & Brunthaler 2004; Sanders et al. 2019; Clarke et al. 2019).

Table 1. Match radius and match rate. "Best" means the closest inside the radius while "All" means all in the radius.

Match radius (")	Best	All	All-Best	Match rate
0.4	16069	16090	21	99.06%
0.3	16027	16032	5	98.80%
0.2	15599	15600	1	96.17%
0.18	15218	15218	0	93.82%
0.16	14630	14630	0	90.19%

(2013):

$$A_I = 0.7465E(V-I) + 1.3700E(J-K). \quad (2)$$

The reddening in the optical regime is $E(V-I) = (V-I) - (V-I)_0 = (V-I) - (M_V - M_I)$. The absolute brightnesses M_V and M_I are computed from the theoretical relations given in Catelan et al. (2004):

$$\begin{cases} M_V = 2.288 + 0.882 \log Z + 0.108(\log Z)^2, \\ M_I = 0.471 - 1.132 \log P + 0.205 \log Z, \end{cases} \quad (3)$$

with the following conversion for metallicity:

$$\log Z = [\text{Fe}/\text{H}] - 1.765, \quad (4)$$

where $[\text{Fe}/\text{H}]$ is defined in Equation 6. We also use the RRL period-luminosity-metallicity (PLZ) relationship from Marconi et al. (2015) to build another distance dataset for cross-check:

$$M_I = -0.07 - 1.66 \log P + 0.17[\text{Fe}/\text{H}], \quad (5)$$

so that we make our results more robust. The reddening $E(J-K)$ was taken from the maps in Gonzalez et al. (2012) which were prepared using the VVV survey (Minitti et al. 2010). We note that, the VVV calibration issue pointed out by Hajdu et al. (2020) does not influence the extinction map. According to Gonzalez et al. (2011), the CASU photometry they started from was re-calibrated using 2MASS, which is different from the "standard photometric source catalogues from VVV that comes from VDFS" as from Hajdu et al. (2020). The comparison of the reddening maps presented in Gonzalez et al. (2012) is furthermore fully consistent with the

most recent PSF photometry from Surot et al. (2019), which was calibrated independently.

Typical statistical error of metallicities and distances are ~ 0.01 dex and 0.15 kpc for the whole sample, among which the (statistical) photometric metallicity error calculated as $d[\text{Fe}/\text{H}] = 0.824 d\phi_{31}$ is the derivative of the formula from Smolec (2005):

$$[\text{Fe}/\text{H}] = -3.142 - 4.902P + 0.824\phi_{31}, \quad (6)$$

where ϕ_{31} is a combination of Fourier parameters $\phi_{31} = \phi_3 - 3\phi_1$. According to Smolec (2005): the metallicity error is calculated as $d[\text{Fe}/\text{H}] = 0.824d\phi_{31}$; the systematic error of the method is about 0.18 dex. The distance error is derived from the error propagation, where the error of $E(V-I)$ and $E(J-K)$ is provided by Nataf et al. (2013) and Gonzalez et al. (2012) respectively.

We cross-match the cleaned sample with Gaia DR2, obtaining a sample of 15,599 sources within a 0.2" match radius. We use the CDS cross-match service, within which the positions are propagated from epoch J2015.5 to J2000 when proper motions are available², to match our OGLE-IV catalog and Gaia data. The match radius is determined as follows: as the OGLE-IV median seeing is $\sim 1''$ (Udalski et al. 2015), the over-match problem is from the Gaia survey to the crowded bulge area. Table 1 shows the match result with different match radii and match modes provided by CDS, "best" means the closest inside the match radius while "all" means all in the match radius. We see 0.2" is where the over-match problem fades away in our field. Overall, the match rate is $\sim 96\%$, which is sufficiently high for us to ignore potential selection bias.

To ensure the Gaia proper motions are reliable, we use the recommended astrometric quality parameter for Gaia DR2³, the re-normalized unit weight error (RUWE) μ , described by Lindegren et al. (2018). A high value of μ may be caused by partially resolved or astrometric binaries. We select sources with $\mu < 1.4$ in our sample (Lindegren et al. 2018), leading to a sample of 12,337 objects. After

² <https://www.cosmos.esa.int/documents/29201/1773953/Gaia+DR2+primer+version+1.3.pdf/a4459741-6732-7a98-1406-a1bea243df79>

³ <https://www.cosmos.esa.int/web/gaia/dr2-known-issues>

this cleaning, we use error propagation from distances and observed proper motions, to obtain the typical error of v_l^* and v_b (as defined in section 3.1.1) $\sim 3.5\%$ and 2.2% respectively.

We adopt the Cartesian coordinate system as described in section 3.1.1 to our sample, which covers $0 \sim 20$ kpc in the x -axis (toward the Galactic centre). The distribution of the cleaned sample is shown in Figure 1 (we only show the $7 \text{ kpc} < x < 10 \text{ kpc}$ part for better visualization, this inner 3 kpc range is also used for more specific research in the bulge region). We use the distance to the Galactic centre determined by Pietrukowicz et al. (2015) (8.27 kpc) for consistency. Figure 2 shows the histogram of the transverse velocities derived from PMs for the whole sample together with two Gaussian best fits. We see the average of $v_b \sim 0$, consistent with Reid & Brunthaler (2004), and the velocity dispersion ratio $\sigma_l/\sigma_b \sim 1.1$, consistent with Sanders et al. (2019).

Other comparison data sets can be found in Table 2. We note that nowadays these catalogs can all be cross-matched with Gaia to obtain proper motions.

3 COMPARISON OF PM AND LOS VELOCITIES AS ROTATION INDICATORS

PM and LOS velocities are both kinematics indicators. Here we will show that the results given by these two indicators are in agreement with each other to show the bulge rotation. We will first use a geometric derivation based on simplest assumptions to give us insights and then validate it with N-body simulations in which the orbits have all the necessary complexity due to the bar. As we will see in Section 4.4, the results from real data also show consistency (see section 4.4).

3.1 Geometrical derivation

3.1.1 Definitions

We set the Sun as the origin of the Cartesian coordinate system, as shown in Figure 3. The x -axis points to the Galactic centre, the y -axis points to the positive direction of Galactic longitude, while the z -axis points to the North Galactic Pole. From the top-down view, the Sun and stars rotate clockwise around the Galactic centre.

Here we discuss a star sample in a small region around the Galactic centre in the bulge. We label its velocity as v_c , which can be decomposed into PM and LOS velocity. We label the Sun-GC distance as R_0 , the distance from the Galactic centre to the line of sight as $R_\perp \equiv R_0 \sin l$, the Sun-stars distance as s , the stars' distance to the Galactic centre as R . We define $d \equiv x - R_0$ (we add negative signs in Figure 3 to make sure all values shown are positive). Other defined angles are labelled in Figure 3. We may simply use $\frac{v_l}{\text{km/s}} \equiv 4.74 \cdot \frac{\mu_l}{\text{mas/yr}} \cdot \frac{s}{\text{kpc}}$ to obtain transverse velocities v_l from longitudinal proper motions μ_l .

When dealing with real data, we transform from the Heliocentric (HC) coordinate to the Galactocentric (GC) coordinate to subtract the solar motion:

$$\begin{cases} v_{\text{los,GC}} = v_{\text{los,HC}} + U_\odot \cos l \cos b \\ \quad + (V_\odot + V_{\text{LSR}}) \sin l \cos b + W_\odot \sin b, \\ v_{l,\text{GC}}^* = v_{l,\text{HC}}^* - U_\odot \sin l \cos b + (V_\odot + V_{\text{LSR}}) \cos l \cos b, \\ v_{b,\text{GC}} = v_{b,\text{HC}} + W_\odot \cos b, \end{cases} \quad (7)$$

where $(U_\odot, V_\odot, W_\odot)$ is the solar peculiar velocity relative to the Local Standard of Rest (LSR). We use the Galactocentric velocity as default.

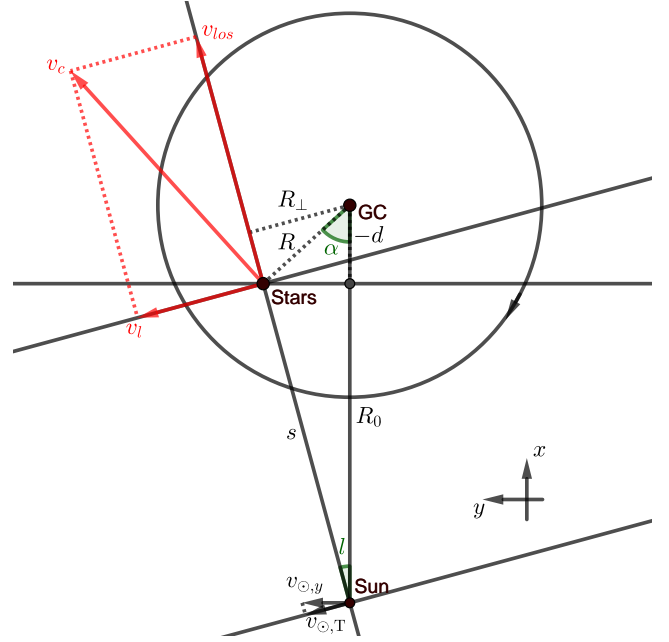


Figure 3. The top-down view from the North Galactic Pole. The red arrows show the circular velocity and its decomposition. The Sun and stars rotate clockwise around the Galactic centre from this view. We define $d \equiv x - R_0$, $R_\perp \equiv R_0 \sin l$.

We note that the dynamics of the inner 5 kpc of the Milky Way disc are strongly influenced by the presence of the Milky Way bar (Eilers et al. 2019), which cannot be simply understood as circular motion, but we can use the simplified case to gain insights.

3.1.2 Discussion about the simplest case

Temporarily ignoring other complexities, here we first use the simplest model (circular, rigid-body motion) to show that PM and LOS velocities can be equivalently used to determine the bulge rotation, then we use mock and real data to demonstrate that the equivalence is still applicable in the real world, where the simplest model is not necessarily valid.

We assume that the system is in equilibrium and that the velocities are near-circular and rigid-body-like. Based on these assumptions, we know that the rotation curves in the bulge region increase linearly with distance to the Galactic centre, which is not a bad approximation according to the rotation curves from previous surveys (Kunder et al. 2012; Ness et al. 2013; Sanders et al. 2019).

In the Galactic plane, the circular velocity for a star is $v_c = \omega R$, where ω is the angular velocity for the rigid-body rotation, R is its distance from the Galactic centre. Next we will obtain the transverse velocity v_l and line-of-sight velocity v_{los} (see Figure 3). For v_{los} , we obtain:

$$v_{\text{los}} = \omega R \sin(\alpha + l) = \omega R_\perp. \quad (8)$$

For v_l , we know:

$$\begin{aligned} v_l &= v_c \cos(\alpha + l) \\ &= \omega R \cos \alpha (\cos l - \tan \alpha \sin l) \\ &= \omega(-d)(\cos l - \tan \alpha \sin l). \end{aligned} \quad (9)$$

What is more, from the geometry, we know:

$$(-d) \tan \alpha = (R_0 + d) \tan l. \quad (10)$$

Table 2. Other surveys for comparison. Now the other catalogs can also be cross-matched with Gaia to generate proper motions. Abbreviations: Multi, multiple populations; RCG, red clump giant; MS, main-sequence object.

Project	References	Population	Observable	Distance	Indicator
OGLExGaia	Our data set	RRLs	PM	yes	$(-v_l^*, d)$
BRAVA	Howard et al. (2008); Kunder et al. (2012)	M giants	LOS velocity	no	$(v_{\text{los}}^*, R_{\perp})$
BRAVA-RR	Kunder et al. (2016)	RRLs	LOS velocity	no	$(v_{\text{los}}^*, R_{\perp})$
ARGOS	Ness et al. (2013)	Multi	LOS velocity	no	$(v_{\text{los}}^*, R_{\perp})$
APOGEE	Zasowski et al. (2016); Ness et al. (2016)	Multi	LOS velocity	no	$(v_{\text{los}}^*, R_{\perp})$
GIBS	Zoccali et al. (2017)	RCGs	LOS velocity	no	$(v_{\text{los}}^*, R_{\perp})$
VVVxGaia	Sanders et al. (2019)	RCGs	PM	yes	$(-v_l^*, d)$
HST SWEEPS	Clarkson et al. (2008, 2018)	MS	PM	yes	$(-v_l^*, d)$

By combining Equation 9 and Equation 10, we obtain:

$$v_l = \omega[(-d) \cos l \cdot (1 + \tan^2 l) - R_0 \tan l \sin l]. \quad (11)$$

Then we have:

$$\begin{cases} \frac{\partial v_{\text{los}}}{\partial R_{\perp}} = \omega, \\ \frac{\partial v_l}{\partial (-d)} = \omega \cos l \cdot (1 + \tan^2 l) \approx \omega. \end{cases} \quad (12)$$

The slopes in two diagrams show the same physical property.

3.2 Validation with mock data

3.2.1 Two simulations

We will now test the consistency between $(-v_l^*, d)$ and $(v_{\text{los}}^*, R_{\perp})$ using mock data from two quite different simulations using different evolutionary histories.

The first is a grid-based N-body simulation by Shen et al. (2010, the Shen model hereafter). For more details about the mock data, see Li & Shen (2012). In the Shen model, 982,889 particles are initially in an unbarred, thin disk. A bar structure emerges during evolution. Then from a bunch of N-body models, they found the one that best matches the BRAVA (Howard et al. 2008) kinematic data after suitable mass scaling. The barred disk evolved from a thin exponential disk that contains $M_d = 4.25 \times 10^{10} M_{\odot}$, about 55% of the total mass at the truncation radius (5 scale lengths). The scale length and scale height of the initial disk are ~ 1.9 kpc and 0.2 kpc, and the length unit of the simulation is this scale length. The classical bulge in this model is less than 8%. The model is consistent with data from several surveys (Kunder et al. 2012; Wegg & Gerhard 2013; Ness et al. 2013; Zasowski et al. 2016).

We also use a second simulation (Athanasoula et al. 2017), as different as possible from the previous one. Contrary to the first simulation described above, this one (N-body+SPH simulation of a barred spiral galaxy as a merger remnant) includes a gaseous component and its physics. Note also that all components, including the dark matter halo, are described self-consistently, and that the initial conditions do not include a disc in equilibrium, but the disc is formed during the simulation and its properties evolve with time. We had at our disposal a large number of such simulations, in all of which a massive merger occurred about 8–10 Gyr ago (e.g., Athanasoula et al. 2016; Peschken et al. 2017). We chose simulation mdf732 which has already been used in two different studies (Athanasoula et al. 2016, 2017). It comprises several stellar components with different properties—i.e. a boxy/peanut bulge, thin and thick disc components, and, to lesser extents, a disky pseudo-bulge,

a stellar halo and a small classical bulge—all cohabiting in dynamical equilibrium. It has a classical bulge with only 9–12 per cent of the total stellar mass and a bar of roughly the correct size, with a boxy/peanut inner part. The mass of each baryonic particle is $10^4 M_{\odot}$, and that of the dark matter ones is $4 \times 10^4 M_{\odot}$, with 10 and 17.5 million particles in each of these components respectively. The snapshot of mdf732 we use consists of 1,052,821 stellar particles.

3.2.2 Mock data setup and reduction

We prepare the mock data from the two simulations with state-of-the-art parameters: we use a Sun-GC distance $R_0 = 8.178$ kpc (Gravity Collaboration et al. 2019), a bar angle $\alpha \sim 27^\circ$ (Cao et al. 2013; Wegg & Gerhard 2013), and the solar near-circular motion with velocity ~ 248 km s $^{-1}$ (Bland-Hawthorn & Gerhard 2016). We use the same Cartesian coordinate system as in section 3.1.1, where the x -axis points towards the Galactic centre.

To be comparable with real data, we select only simulation particles in the region $(-10^\circ < l < 10^\circ, -7^\circ < b < -2.5^\circ, x > 0)$, where $x > 0$ means the line of sight is toward the Galactic centre but not the anti-centre) including Baade’s Window, leading to a sample of 47,683 particles (the Shen model) and 37,342 particles (mdf732) respectively.

3.2.3 Comparison of the two rotation indicators

We compare these two indicators in Figure 4. We label both R_{\perp} and d as ‘Distance’ for the x -axis, and label both v_{los} and $(-v_l^*)$ as ‘Velocity’ for the y -axis. We see both mock datasets show the consistency between two indicators. If we use a different Galactic longitude cut (i.e. different disc contamination), the consistency still holds.

3.3 Results with real data

In Table 2, we list some kinematic surveys of the Galactic bulge stars. None of these surveys uses both indicators, because we can rarely obtain $(-v_l^*, d)$. Before Gaia DR2, PM surveys to the bulge were rare, and it is always hard to obtain the distance from bulge stars. Clarkson et al. (2018) tried to use PM to describe the rotation of stars in the bulge. However, their accuracy of distance is too poor to give a quantitative description. Thanks to Gaia DR2 and the distance determination of VVV RCGs, the equivalence can be validated by the consistency of the green line and blue & red lines as shown in section 4.4, where they describe similar populations and show consistency using different indicators.

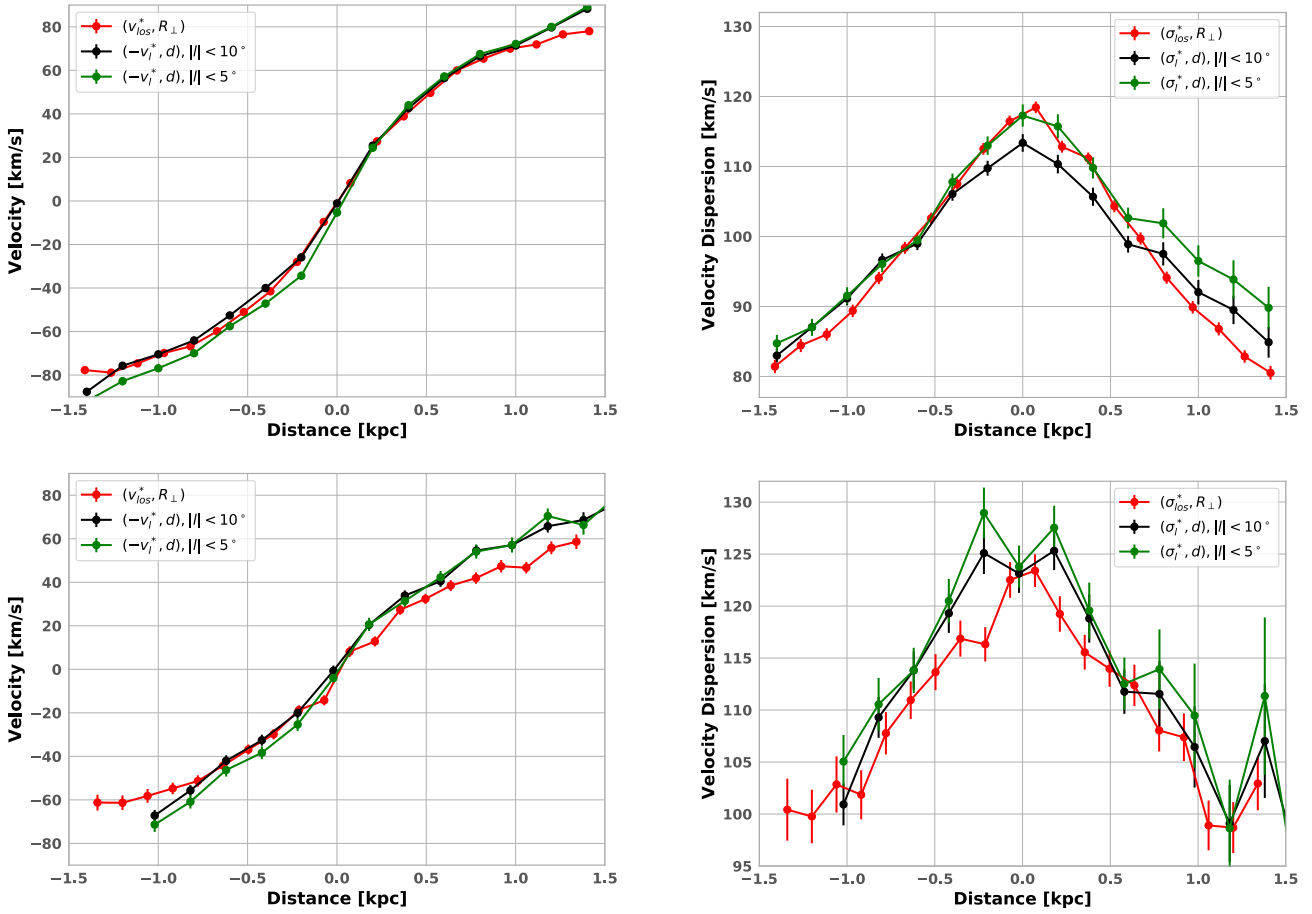


Figure 4. Comparison of two bulge rotation indicators (v_{los}^* , R_{\perp}) (red) and $(-v_l^*$, d) (green and black) based on the mock data of two simulations. The 'Distance' as x -axis is R_{\perp} or d which are defined in Figure 3, the 'Velocity' as y -axis is v_{los}^* or $(-v_l^*)$. Top panels present results from the Shen model, while bottom panels are from mdf732. Here we use different cut in l to visualize the influence of disc contamination on the results.

4 RESULTS

In this section, we quantitatively measure the angular velocity of the RRLs as a distinct slow-rotating, kinematically-hot population in the Galactic bulge, and show solid evidence of the multi-component nature of RRLs, which might explain some previous disputes.

In this paper, we use the term 'angular velocity' to describe the slope of the rotation curve, which is not the same as the bar pattern speed. The angular velocities are obtained in the inner 1.5 kpc with linear fitting to the *Velocity-Distance* diagrams: for the data points ranging $-1.5 \text{ kpc} \sim 1.5 \text{ kpc}$ in the x -axis, we use the least-squares method to find the best fit; the errors are obtained by the square root of the diagonal elements of the covariance matrix.

In particular, the errors of distances, $[\text{Fe}/\text{H}]$ and PM are applied with Gaussian resampling as follows: for each value, we create a Gaussian distribution whose mean and error are as observed. For the rotation curves, the error bars are generated with bootstrap with 100,000 samples; for each (re-)sample, we use different, newly-created distances for all stars obeying Gaussian distributions. For the star-count map, we replot it ten more times with newly-created distances to check the influence of distance uncertainty on the bar angle. We use similar method applying the error of $[\text{Fe}/\text{H}]$ and PM.

4.1 Cylindrical rotation

We compare the rotation curves at different Galactic latitudes in the left panel of Figure 5. We also add the catalog from Gran et al. (2016, cross-matched with Gaia DR2) which is a VVV extension program on high Galactic-latitude bulge RRLs ($-10.3^\circ \lesssim b \lesssim -8.0^\circ$, $-10.0^\circ \lesssim l \lesssim +10.7^\circ$). To determine the distances, Gran et al. (2016) used the (adapted) period-luminosity-metallicity (PLZ) relation (Alonso-García et al. 2015), which modified the PLZ relationship of Catelan et al. (2004) to the VIRCAM/VISTA filter system; they applied extinction law from Cardelli et al. (1989). We note that their determined-distances might be more significantly influenced by VVV photometric calibration issue (Hajdu et al. 2020).

Figure 6 shows the metallicity and 2D velocity (we define as $\sqrt{(v_l^*)^2 + v_b^2}$) distributions in different Galactic latitudes. We see the change of the metallicity and the 2D velocity is mild among different latitudes in our fields. From the velocity distribution shown in the right panel of Figure 6, we identify high-velocity stars by requiring them to be $> 2.5\sigma_{2D}$. We find this fraction is about 2%, roughly a factor of 3.5 smaller than the high-velocity star fraction identified in 3D by Kunder et al. (2020). We are not sure whether this can be well explained by the difference between 2D and 3D velocities. We return to this issue briefly in the conclusion section.

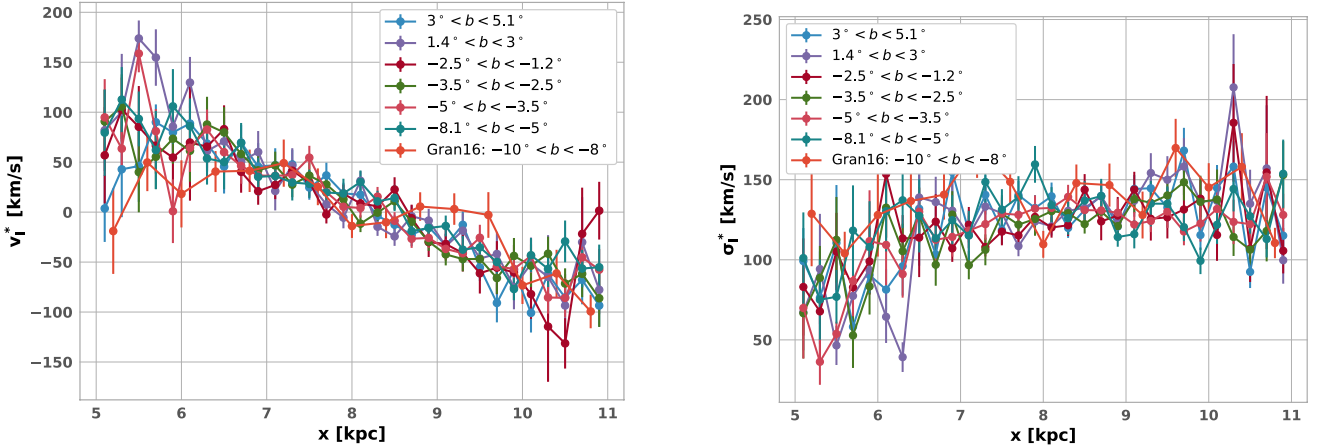


Figure 5. Left panel: Cylindrical rotation of RRLs in different Galactic latitude bins. We divide OGLExGaia data into six bins, including both North and South of the Galactic plane. We also add the sample from a VVV extension program (Gran et al. 2016) as completion in high Galactic latitude (labelled as Gran16). The similarity of rotation curves of RRLs in different Galactic latitudes argues for a cylindrical rotation nature, which is similar to the findings from previous surveys on younger populations using LOS velocities (e.g., Kunder et al. 2012; Ness et al. 2013; Zasowski et al. 2016; Zoccali et al. 2017). Right panel: Velocity dispersion for the same samples. We also find the absence of the central peak of the velocity dispersion diagram near the Galactic plane ($|b| < 5^\circ$), which is similar to metal-poor RCGs (Ness et al. 2013, their Figure 6).

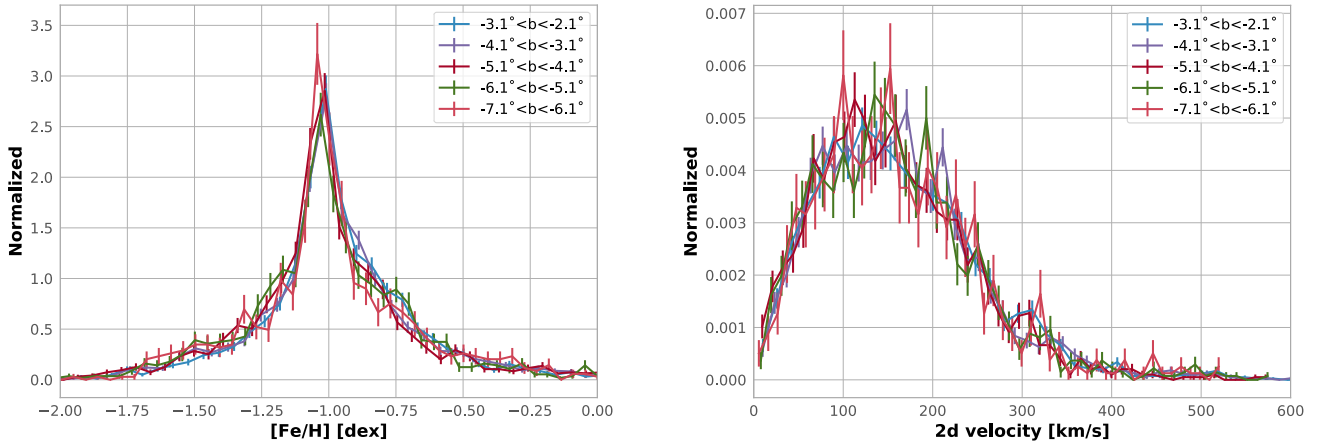


Figure 6. Left: metallicity distribution in different Galactic latitudes. Right: 2D velocity (we define as $\sqrt{(v_l^*)^2 + v_b^2}$) distribution in different Galactic latitudes. We see the change of the metallicity and the 2D velocity is mild among different latitudes in our fields. The error bars are Poisson noise.

One associated question is whether the slow-rotating and kinematically-hot nature of bulge RRLs is totally caused by the high-velocity stars. We checked the results with and without them (i.e., the results shown in Figures 11 cyan lines), to find this effect do not compensate the high-velocity-dispersion nature; also, the trend of the rotation curve do not change with such cleaning.

Many previous surveys like BRAVA, ARGOS, APOGEE, GIBS have shown the cylindrical rotation nature of younger stellar populations using LOS velocities. This, however, is the first time that the cylindrical rotation of the Galactic bulge is revealed from PMs.

An interesting fact worth mentioning in the right panel of Figure 5 is that there is no central peak, not even for $|b| < 3^\circ$, which is not the case of younger populations (for example, M-type Giants in Kunder et al. 2012, their Figure 11). This is similar to, but more

pronounced than what is found for the metal-poor RCGs (Ness et al. 2013, their Figure 6).

4.2 Rotation of old sub-populations

The multi-component nature of bulge RRLs has been raised recently by Pietrukowicz et al. (2015, they found two distinct sequences of RRab variables in the period-amplitude diagram.) and Dékány et al. (2018, they found the metallicity distribution function of RRab variables can be fit with multiple Gaussian distributions.).

Here we use the metallicity provided by Pietrukowicz et al. (2015). Pietrukowicz et al. (2015, their Figure 17) shows a sharp and symmetric distribution of RRLs around $[\text{Fe}/\text{H}] \sim -1$. We thus split our sample in two and obtain the rotation curves shown in the left panel of Figure 7. We also add the result from Sanders et al. (2019, their Figure 4) who also used PM data from Gaia DR2.

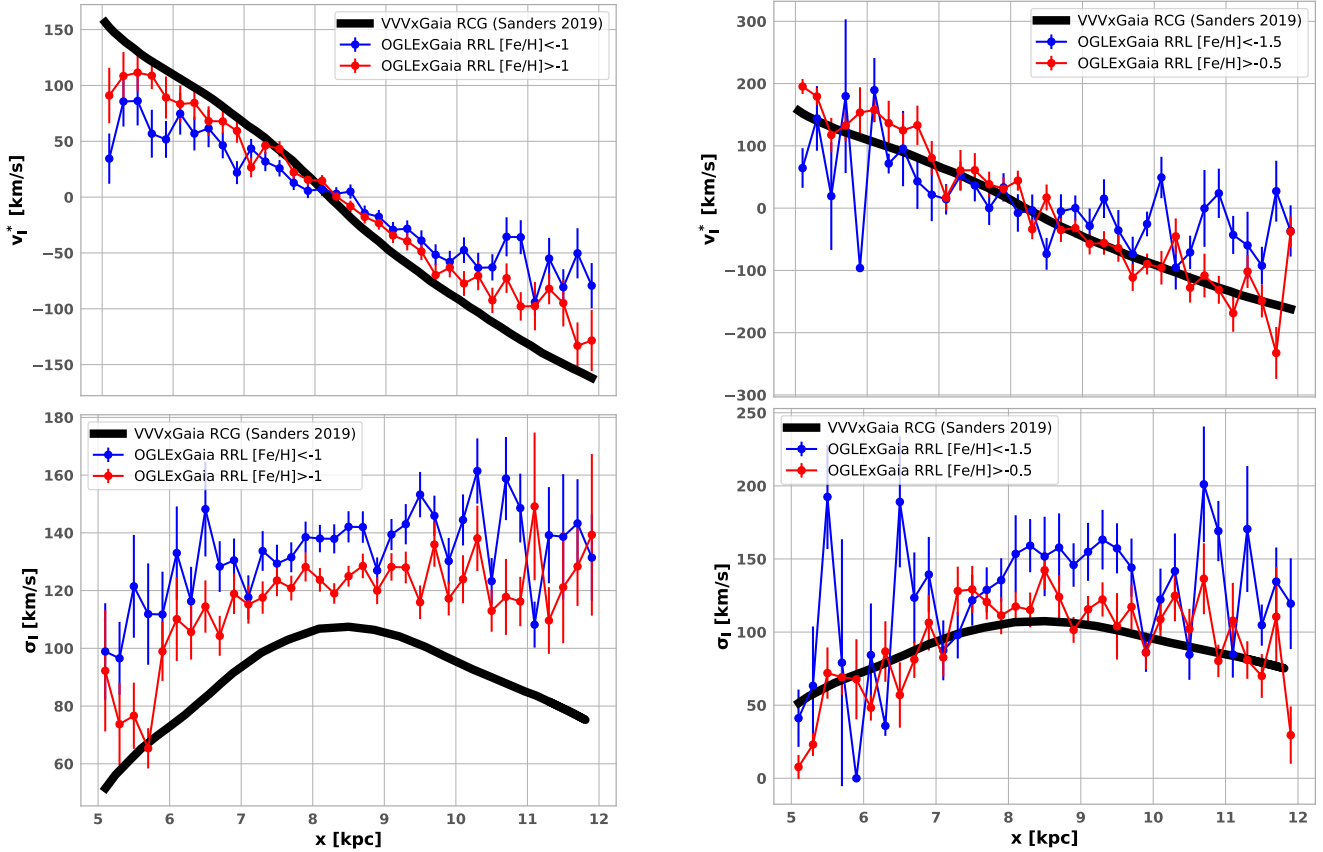


Figure 7. Left panel: rotation (above) and velocity dispersion (below) of metal-poor (blue, $[\text{Fe}/\text{H}] < -1$) and metal-rich (red, $[\text{Fe}/\text{H}] > -1$) RRLs. We also add the corresponding curve for RCGs from Sanders et al. (2019) for comparison. All the rotation curves are based on the PM from Gaia DR2. The angular velocity of metal-poor RRLs ($[\text{Fe}/\text{H}] < -1$), metal-rich RRLs ($[\text{Fe}/\text{H}] > -1$) and RCGs are respectively (32.42 ± 1.48) , (40.29 ± 2.28) and (55.07 ± 0.63) $\text{km s}^{-1} \text{kpc}^{-1}$. Right panel: as in the left panels, but we now split the sample with stricter restrictions on metallicity. We see RRLs with $[\text{Fe}/\text{H}] > -0.5$ show properties similar to RCGs. The angular velocity for RRLs with $[\text{Fe}/\text{H}] < -1.5$ and $[\text{Fe}/\text{H}] > -0.5$ are respectively (26.77 ± 8.39) $\text{km s}^{-1} \text{kpc}^{-1}$, (61.76 ± 6.26) $\text{km s}^{-1} \text{kpc}^{-1}$.

We see that the metal-poor RRLs rotate the slowest and have the largest velocity dispersion. RCGs, as the main part of the Galactic bulge (Ness et al. 2013), rotate the fastest and are the most kinematically cold. It seems the metal-rich RRLs are intermediate between metal-poor RRLs and RCGs. Quantitatively, the angular velocity of metal-poor RRLs ($[\text{Fe}/\text{H}] < -1$), metal-rich RRLs ($[\text{Fe}/\text{H}] > -1$) and RCGs are respectively (32.42 ± 1.48) , (40.29 ± 2.28) and (55.07 ± 0.63) $\text{km s}^{-1} \text{kpc}^{-1}$.

We next split the sample again by metallicity, but now considering separately the RRLs with $[\text{Fe}/\text{H}] < -1.5$ and $[\text{Fe}/\text{H}] > -0.5$ shown in the right panel. We see that the latter group of RRLs show similar properties to RCGs.

We note that the fact that metal-poorer stars in the Galactic bulge rotate slower and are kinematically-hotter has been observed by several previous bulge surveys for other populations (Ness et al. 2013, 2016; Zoccali et al. 2017; Rojas-Arriagada et al. 2017; Clarkson et al. 2018; Arentsen et al. 2020). This has also been reproduced by N-body chemo-dynamic simulations (Athanasoula et al. 2017).

4.3 Spatial distribution

There has been a debate on whether bulge RRLs trace the bar structure. The bar angle determined using near-IR VVV observations of

OGLE-III bulge RRLs by Dékány et al. (2013) is $12.5^\circ \pm 0.5^\circ$, while optical observations of OGLE-IV bulge RRLs by Pietrukowicz et al. (2015) gave a bar angle $20^\circ \pm 3^\circ$. We will use our sample to shed further light on this point. For the spatial distribution, we need not use Gaia data, so we use the dataset (15,599 sources) uncleaned with the Gaia RUWE flag to maintain the completeness of the RRab stars.

We plot the distribution of bulge RRLs from a top-down view. The left panel in Figure 8 is from Wegg & Gerhard (2013, their Figure 17) showing the surface density obtained for RCGs from the VVV survey; the right panel shows the surface density map from our data with the following operations:

- We restrict the region to $-6.5^\circ < b < -2.8^\circ$, $-1 \text{ kpc} < y < 1 \text{ kpc}$, $7 \text{ kpc} < x < 10 \text{ kpc}$ to avoid the incomplete fields of the survey.
- We segment the region into square cells of the size of 0.1 kpc from the top-down view. The color of each cell is determined by the star counts in a circle with a radius of 0.15 kpc centred in the cell's centre. The star counting region for each cell is larger than the cell itself for better statistics. This operation is similar to *smoothing* in image reduction.
- Note that we consider the cone effect, i.e., multiply the count in each cell by a factor $1/s^2$ where s is the star-Sun distance.

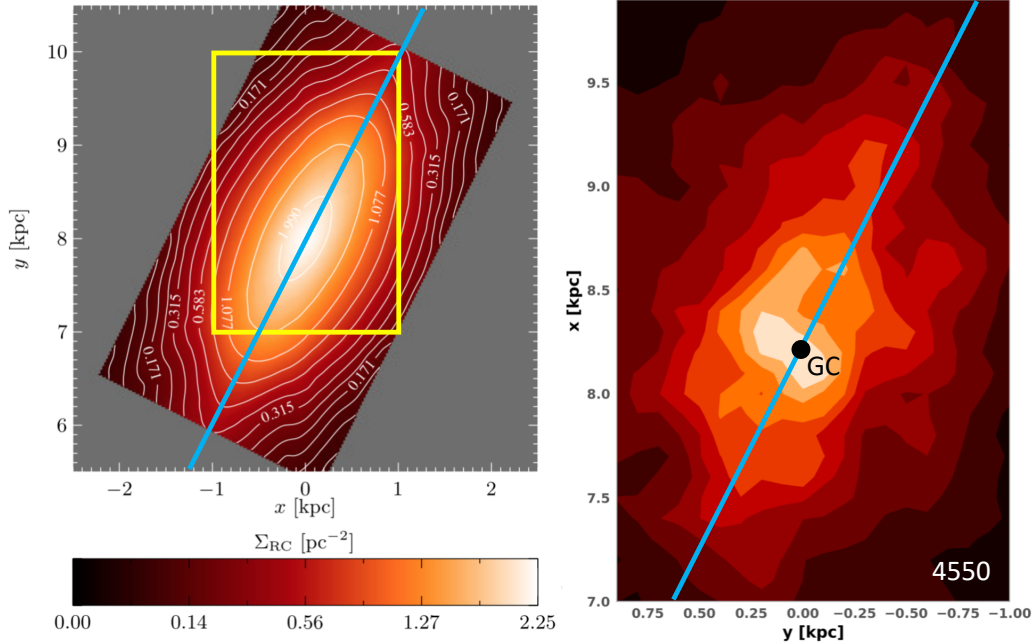


Figure 8. Surface density of RCGs (left panel, from Wegg & Gerhard 2013, their Figure 17) and RRL stars (right panel). The yellow rectangle in the left panel shows the region covered by the right panel. The blue lines in both panels show an angle $\sim 27^\circ$, the RCG bar angle obtained from VVV (Wegg & Gerhard 2013). The right panel shows that this value is a reasonable approximation of the bar angle of our RRL distribution. The number in white in the bottom right corner of the right panel is the total number of the stars used here. The location of the Galactic centre is given by a black filled circle (GC).

We find a bar angle (α) for RRLs $\sim 27^\circ$, which is close to earlier determinations for younger populations, like VVV Type II Cepheids ($\sim 30^\circ$, Dékány et al. 2019), Gaia bulge Miras ($\sim 21^\circ$, Grady et al. 2020), VVV RCGs ($20^\circ - 30^\circ$, Simion et al. 2017), OGLE RCGs ($29^\circ \pm 2^\circ$, Cao et al. 2013; $27^\circ \pm 2^\circ$, Wegg & Gerhard 2013; $25^\circ \pm 2^\circ$, Rattenbury et al. 2007; $20^\circ - 30^\circ$, Stanek et al. 1997), 2MASS red giant star counts ($20^\circ - 35^\circ$, López-Corredoira et al. 2005), and modeling the asymmetry of the COBE NIR photometry ($25^\circ \pm 10^\circ$; Dwek et al. 1995, Binney et al. 1997, Fux 1999, Bissantz & Gerhard 2002).

We next adopt the same instruction separately to the metal-poor ($[\text{Fe}/\text{H}] < -1$) and the metal-rich ($[\text{Fe}/\text{H}] > -1$) shown in Figure 9. We see that the metal-poor RRLs show a smaller bar angle, which is in agreement with the bar angle measured by Dékány et al. (2013) and Minniti et al. (2017), who did not cut the metallicity. So the discrepancy of the two bar angles of RRLs might be explained by the selection bias due to different metallicity ranges. We note that their sample is smaller, and may suffer from VVV photometry calibration issues (Hajdu et al. 2020). Currently, their data are being re-analyzed by Dékány (2020, private communication).

We use the Gaussian resampling method mentioned at the beginning of section 4 to confirm that structures in the star-count maps are not significantly influenced by the error of distances. We also used another distance dataset determined using period-luminosity-metallicity (PLZ) relationship from Marconi et al. (2015) instead of Catelan et al. (2004), the distribution discrepancy of metal-poor and metal-rich RR Lyraes still holds.

Figure 10 shows the vertical volume number density distribution of the bulge RRLs at the Galactic centre. We calculate the density as follows: we select a rectangle field ($-4.2^\circ < l < 4.2^\circ$, $-6.8^\circ < b < -2.8^\circ$) to ensure the field is all covered in our

sample, then we get a cuboid which is in that field and is located at the Galactic centre:

$$\begin{cases} x_1 < x < x_2, \\ x_1 \tan l_1 < y < x_1 \tan l_2, \\ x_1 \tan b_1 < z < x_2 \tan b_2, \end{cases} \quad (13)$$

where we use $x_1 \equiv 8.0$ kpc, $x_2 \equiv 8.5$ kpc, $l_1 \equiv -4.2^\circ$, $l_2 \equiv 4.2^\circ$, $b_1 \equiv -6.8^\circ$, $b_2 \equiv -2.8^\circ$. We cut $\delta z \equiv 0.06$ kpc in z -direction for each slice, for which we obtain the volume:

$$V = (x_2 - x_1)(y_2 - y_1)\delta z.$$

The volume number density is then obtained by $n = N/V$. The error bars are Poisson noise. We apply a similar workflow to the Gran et al. (2016) data. As shown in Figure 10, the vertical density of bulge RRLs follows an exponential distribution with a scale height $h_z = 0.29 \pm 0.06$ kpc. We note that the exponential scale length of the Galactic bar in z -direction traced by RC stars is ~ 0.25 kpc (Cao et al. 2013), indicating that the bulge RRLs follow the similar distribution of the majority of the bulge stars. The completeness of the RRab stars was discussed in Soszyński et al. (2014, 2019); Gran et al. (2016), concluding that the RRab stars in these fields are sufficiently complete to do such statistics.

4.4 Comparison of rotation curves

In Figure 11, we apply the equivalence of indicators described in section 3 to the surveys from Table 2. Given the cylindrical rotation nature of RRLs, we can combine RRLs from different Galactic latitudes together.

As mentioned in section 3.3, the consistency (see Figure 11)

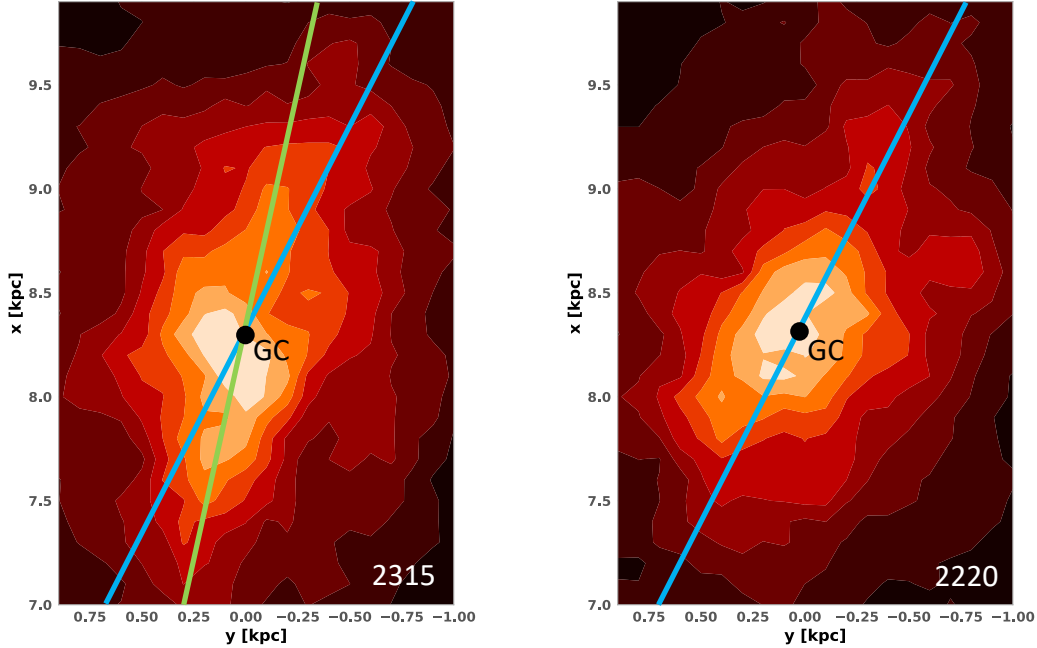


Figure 9. As the right panel of Figure 8, but after splitting our sample by metallicity. The left panel is for metal-poor RRLs ($[\text{Fe}/\text{H}] < -1$), and the right panel is for metal-rich ones ($[\text{Fe}/\text{H}] > -1$). The blue lines show an angle $\sim 27^\circ$, and the green line shows a bar angle $\sim 12^\circ.5$, as given by [Dékány et al. \(2013\)](#). We see that the bar angle for the metal-poor RRLs is smaller. Selection biases from different metallicity ranges can explain previous disagreements on the bar angle obtained from bulge RRLs (see section 3.1.2).

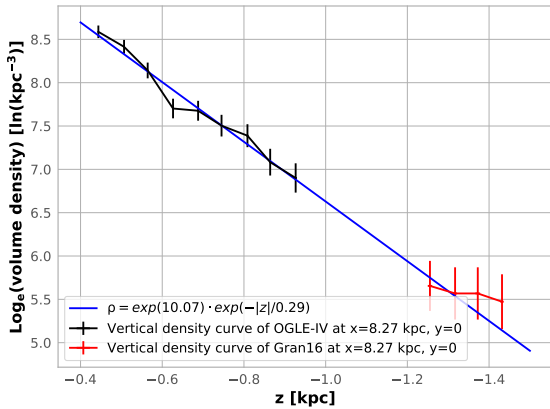


Figure 10. The vertical volume number density distribution in \ln of the bulge RRLs. The vertical density of bulge RRLs follows an exponential distribution with a scale height $h_z = 0.29 \pm 0.06$ kpc. We note that the exponential scale length of the Galactic bar in z -direction traced by RC stars is ~ 0.25 kpc ([Cao et al. 2013](#)), indicating that the bulge RRLs follow similar vertical profile to the majority of the bar stars.

of VVVxGaia (green line) and BRAVA & APOGEE (blue & red line) is also a validation for the equivalence of the two indicators ($-v_l^*$, d) and $(v_{\text{los}}$, R_\perp): they describe similar populations and show similar properties.

RRLs show a significantly different behavior from RCG and M giants to which we compare them in Figure 11. This is presumably due to the fact that they are a different population with slower

Table 3. Angular velocities derived from rotation curves.

Survey	Population	Indicator	Ang. Vel. [$\text{km s}^{-1} \text{kpc}^{-1}$]
OGLExGaia	RRLs	$(-v_l^*, d)$	36.95 ± 1.05
VVVxGaia	RCGs	$(-v_l^*, d)$	55.07 ± 0.43
BRAVA	M giants	$(v_{\text{los}}, R_\perp)$	64.11 ± 5.43

rotation and are kinematically hotter, as found previously ([Kunder et al. 2016](#); [Contreras Ramos et al. 2018](#)). The angular velocities derived from the rotation curves are shown in Table 3. The angular velocity of RRLs ($35 \text{ km s}^{-1} \text{kpc}^{-1}$) is consistent with [Wegg et al. \(2019\)](#) in which the rotation speed of RRLs at the distance of 1.5 kpc from the Galactic centre is $\sim 50 \text{ km s}^{-1}$. Also, it is worth mentioning here the fact that the metal-poor bulge stars rotate slower has been observed by several previous surveys ([Ness et al. 2013, 2016](#); [Zoccali et al. 2017](#); [Rojas-Arriagada et al. 2017](#); [Clarkson et al. 2018](#); [Arentsen et al. 2020](#)). [Ness et al. \(2013\)](#) mentioned that the slower rotation in their metal-poor sample may be caused by stars of the metal-weak thick disc and halo which presently lie in the inner Galaxy, which might also explain the behaviour of bulge RRLs.

We then restrict the RRLs to those within the innermost 0.9 kpc in order to compare with [Kunder et al. \(2020\)](#); we take the value 0.9 kpc from their Figure 6, which they treated as a central/classical bulge region. In our sample, the trend of RRLs does not change significantly with this constraint, and the velocity dispersion with such constraint is still significantly larger than younger populations. The difference between the two is that in [Kunder et al. \(2020\)](#), stars with apocenter distances > 3.5 kpc were not included; the exclusion of these stars also decreases the velocity dispersion reported in the

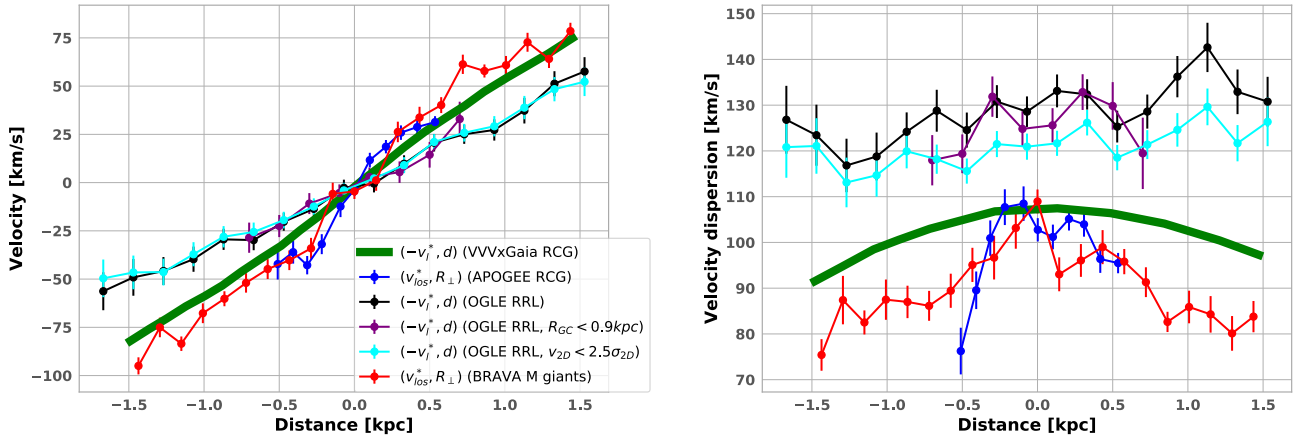


Figure 11. Left panel: Rotation curves from several surveys, the cross-match radius with Gaia DR2 is $0.2''$ cleaned with $\text{RUWE} < 1.4$. RRLs (black line) clearly rotate slower. The angular velocity (the slope of rotation curves fit in the inner 1.5 kpc) derived from VVVxGaia (Sanders et al. 2019), OGLExGaia and BRAVA (Kunder et al. 2012) are respectively (55.07 ± 0.43) , (36.95 ± 1.05) , (64.11 ± 5.43) $\text{km s}^{-1} \text{kpc}^{-1}$ (see Table 3). The consistency of the green line and the blue & red lines is also a validation for the equivalence of these two indicators. Right panel: bulge RRLs are kinematically hotter than other populations. Here the *Distance* as *x*-axis is R_{\perp} or d as defined in Figure 3. We then restrict RRLs to those within the inner 0.9 kpc (purple line), or exclude high-velocity stars (cyan line) to check their influence (to compare with Kunder et al. 2020). We find that the rotation trend does not change significantly.

Kunder et al. (2020) RRL dispersion as compared to what is found here. We will return to this issue briefly in the conclusion section.

5 DISCUSSION

5.1 The equivalence of PM and LOS velocities from the dynamics point of view

A further point that needs to be discussed here is our finding that PM and LOS velocities can be indiscriminately used to study the rotation in the bulge region of our Galaxy. This can be shown (see section 3.1) in a simple, geometric way under the following two assumptions: The system is in equilibrium, the backbone, main periodic orbits in the region under consideration are not far from circular, and the rotation in the inner parts increases linearly with distance from the centre. The first and third of these assumptions should not present any difficulties. The second one, however, namely that the orbits can be described by circles, needs further discussion as it is by now well established that our Galaxy is barred, and we are modeling the inner regions. For this reason, we used mock data from two independent simulations, which we chose to be as different as possible (see section 3.2.1). Although the snapshots we chose are barred, we found that, contrary to what one would have naively expected, our two rotation indicators can be indiscriminately used in both models.

To understand this, one must remember that the region we are studying here is not the whole bar, but only its centre-most part, i.e., stars which are at a distance of $1 - 2$ kpc only from the centre, or, equivalently, less or of the order of half the bar length. At such distances, the amplitude of the $m = 2$ and of the higher even Fourier components ($m = 4, 6, 8, \dots$) of the surface density distribution, are much lower than somewhat further out, as has been shown both by observations (e.g., Buta et al. 2006) and simulations (e.g., Athanassoula & Misiriotis 2002). This argument can be pushed further by looking at the shape of the main periodic orbits in that region. Indeed, Athanassoula (1992, their Figure 9) gives information on the

shape of these periodic orbits⁴ and shows that their elongation is relatively small near the centre, then increases with increasing distance from the centre to reach a maximum and then drops in the outer parts of the bar. Of course, the axial ratio of these orbits will depend on the gravitational potential and particularly on the shape of the iso-potentials in the central regions, so that it is not possible, from these orbits only, to make any quantitative statements for the inner part of the Galactic bar. Qualitatively, however, our arguments here show that the rotation obtained by PM and LOS velocities can be equivalent, even when the bar is present.

5.2 Why was the rotation of bulge RRLs not previously observed quantitatively?

Independent observations from BRAVA-RR (Kunder et al. 2016) and VVV (Contreras Ramos et al. 2018) show that bulge RRLs are non-rotating or slow-rotating. We demonstrate that this is qualitatively, but not quantitatively, consistent with our results.

The BRAVA-RR presented by Kunder et al. (2016) is an extension program of BRAVA, which focused on the RRLs in the Galactic bulge with LOS velocities. The sample of 947 sources was selected from OGLE-III RRL catalog, whose field is shown in Kunder et al. (2016, their Figure 1) ranging $-5^{\circ} \leq l \leq 5^{\circ}$, $-5.5^{\circ} \leq b \leq -1^{\circ}$. Figure 12 is prepared as follows: after cross-matching BRAVA-RR with Gaia DR2, we obtain a sample of 862 RRLs with 6D phase space information. Then we can use both indicators ($v_{\text{los}}^*, R_{\perp}$) and $(-v_l^*, d)$ to obtain the angular velocity. We see, within error bars, the blue line is consistent with the other two curves. Because the BRAVA-RR curve (red) is too close to the Galactic centre, $(v_{\text{los}}^*, R_{\perp})$ is not a good indicator to reflect the rotation. In the right panel of

⁴ This work concerns the two main families of periodic orbits at the centre, namely the $x1$ and the $x2$, therefore, also the orbits trapped around them. Such information does not yet exist for higher multiplicity periodic orbits, but their importance in the dynamics of this inner region is also not yet established.

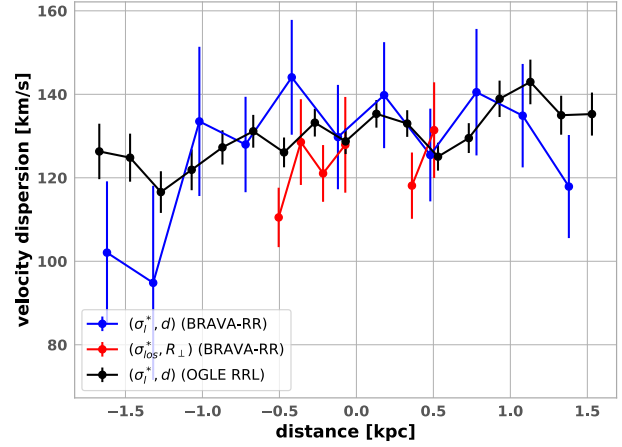
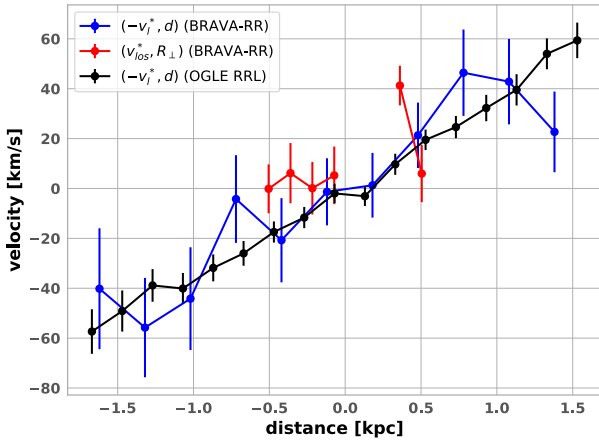


Figure 12. We show why [Kunder et al. \(2016\)](#) have not observed the rotation. Their sample is too close to the Galactic centre (l range is too small) so that v_{los} is not a good indicator to reflect the rotation. The blue line is the 6D sample obtained after cross-matching BRAVA-RR and Gaia DR2, showing consistency with both BRAVA-RR and ours (black line).

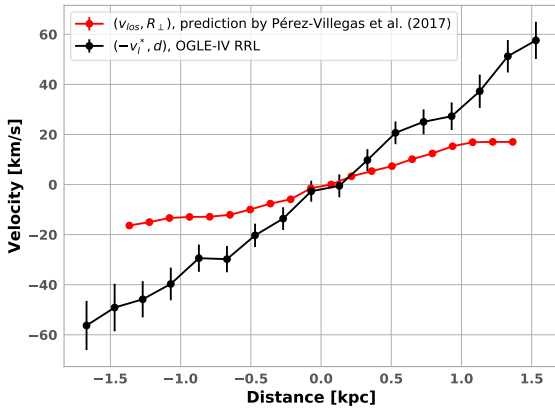


Figure 13. The simulation by [Pérez-Villegas et al. \(2017\)](#) reproduced the BRAVA-RR ([Kunder et al. 2016](#)) data. The assumption of [Pérez-Villegas et al. \(2017\)](#) is that RRLs in the Galactic bulge are inner halo stars; the predicted rotation is too slow to be in agreement with the rotation curve based on Gaia proper motions.

Figure 12, we plot the corresponding velocity dispersion curves and show again that the three curves are consistent with each other.

Figure 13 shows the rotation curve for the inner stellar halo, as predicted by a simulation of [Pérez-Villegas et al. \(2017\)](#) and obtained from the Gaia proper motions. We extracted the values from the bottom left panel of their Figure 3. We also added our result from Figure 11. We see there is a considerable difference between the two, which could well indicate that the RRL population of the Galactic bulge is not necessarily consistent with being the inward extension of the Galactic metal-poor stellar halo. We note that the inconsistency between the simulation in [Pérez-Villegas et al. \(2017\)](#) and Gaia observation was also mentioned by [Wegg et al. \(2019\)](#).

Another piece of evidence stating their non-rotating RRL paradigm is provided by [Contreras Ramos et al. \(2018, their Figure 13\)](#), based on VVV data. Their RRL identification is made by an au-

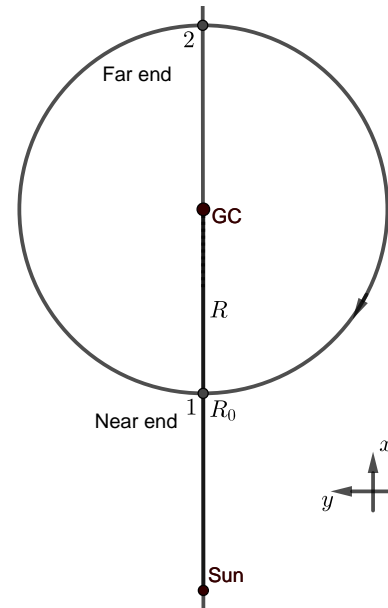


Figure 14. A simplest view from the North of Galactic plane to understand the trend in the μ_I -distance diagrams, so that to explain why [Contreras Ramos et al. \(2018\)](#) did not find the rotation.

tomated RRL classifier based on machine learning ([Elorrieta et al. 2016](#)) and its modified version ([Contreras Ramos et al. 2018, their appendix](#)). Their sample of 959 RRLs in the field $|l|, |b| \lesssim 1.7^\circ$ is too close to the disk to be cross-matched with Gaia DR2.

As shown in [Contreras Ramos et al. \(2018, their Figure 13\)](#), they use μ_I^* as the y -axis and W_{K_s} -band magnitude as the x -axis, fitting the sample of stars with a horizontal line. However, this does not support their non-rotating interpretation but supports our scenario.

To understand this better, firstly we take the observables into

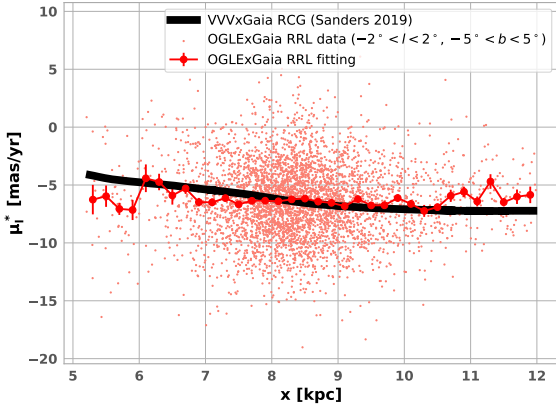


Figure 15. Proper motions of RRLs and RCGs in the bulge. We compare this to Contreras Ramos et al. (2018, their Figure 13); the horizontal trend in the bulge region (7~10 kpc) reflect a rotating sample with similar angular velocity to the Sun's around the Galactic centre.

Equation 11. Of the solar motion (see Figure 3), we know that:

$$v_{\odot,y} \equiv |\mu_{GC}| \cdot R_0, \quad (14)$$

$$\mu_l \cdot s = v_l - v_{\odot,T} = v_l - v_{\odot,y} \cos l,$$

where $v_{\odot,y}$ is the solar tangential velocity around the Galactic centre and $|\mu_{GC}| = 30.24 \text{ km s}^{-1} \text{ kpc}^{-1} = -\mu_{GC}$ is the proper motion of the Galactic centre, $v_{\odot,T}$ is the tangential velocity with respect to the line of sight (see Figure 3). We have:

$$v_l = \mu_l \cdot s + |\mu_{GC}| \cdot R_0 \cos l. \quad (15)$$

Then we take the simplest case into consideration (see Figure 14, see also Qin et al. 2015, their section 3.5) for a qualitative conclusion. When we look along the Sun-GC line on the Equatorial Plane ($l = 0, b = 0, \alpha = 0$ or 180°), For stars on pure circular orbits, the PM of the stars in the near-end and far-end are:

$$\mu_{l,1} = \frac{\mu_{GC} \cdot R_0 + \omega \cdot R}{R_0 - R} \quad (16)$$

$$\mu_{l,2} = \frac{\mu_{GC} \cdot R_0 - \omega \cdot R}{R_0 + R},$$

where $\mu_{GC} = -6.38 \text{ mas/yr} = -30.24 \text{ km s}^{-1} \text{ kpc}^{-1}$. Here we can see, for a rigid body rotation with angular velocity ω , that there will be three cases:

- In the case of $\omega = |\mu_{GC}| = -\mu_{GC}$, we will obtain $\mu_{l,1} = \mu_{l,2} = \mu_{GC} = -6.38 \text{ mas/yr}$, or a horizontal line in the μ_l -distance diagram.
- For $\omega > |\mu_{GC}|$, $\mu_{l,1} > \mu_{GC} > \mu_{l,2}$, we obtain a descending trend in the μ_l -distance diagram.
- If $\omega < |\mu_{GC}|$, $\mu_{l,1} < \mu_{GC} < \mu_{l,2}$, we obtain an ascending trend in the μ_l -distance diagram.

Our angular velocity of bulge RRLs ($36.95 \pm 1.05 \text{ km s}^{-1} \text{ kpc}^{-1}$) is slightly larger than that of $|\mu_{GC}|$, which is close to the first case. We can also check this with our data in Figure 15, in which the horizontal trend in the bulge region (7~10 kpc from the Sun) reflects a rotating sample with similar angular velocity to the Sun's rotation around the Galactic centre.

Moreover, as similarly explained in section 4.3, the fact that the rotation of bulge RRLs was not clearly observed might also be explained by the selection bias on metallicity; extremely metal-poor RRLs show mild rotation.

6 CONCLUSION

Spectroscopic surveys of the Galactic bulge region show that this component has a complex chemodynamical structure (Barbuy et al. 2018, and references therein). In our work, "bulge" is a general concept referring to the specific Galactic centre region (sometimes referred to as the "inner Galaxy"). We provide a phenomenological view of the RRLs in the inner Galaxy region for a better understanding of their nature.

The proper motions have been, so far, rarely used to obtain the rotation curve in the Galactic bulge due to their measurement difficulty. Thanks to the data release 2 of Gaia and the OGLE-IV RRLs with distance determination, we can now use PM to demonstrate the bulge rotation and compare it with previous LOS velocities. We summarize our results as follows:

- We show the equivalence of PM and LOS velocities as the Galactic bulge rotation indicators, which has not been discussed in previous works.
- Metal-poor and metal-rich RRLs show different behaviors: 1) their angular velocities are different. As seen in Figure 7, this is $(32.42 \pm 1.48) \text{ km s}^{-1} \text{ kpc}^{-1}$ for $[\text{Fe}/\text{H}] < -1$ and $(40.29 \pm 2.28) \text{ km s}^{-1} \text{ kpc}^{-1}$ for $[\text{Fe}/\text{H}] > -1$; 2) their spatial distributions are different, the metal-rich RRLs show a similar triaxial structure to that of RCGs while the metal-poor ones show a smaller bar angle. This provides a view to explain the conflict between Dékány et al. (2013) and Pietrukowicz et al. (2015); 3) extremely metal-rich RRLs ($[\text{Fe}/\text{H}] > -0.5$) show similar behavior as RCGs.
- We update the results of Kunder et al. (2016) and Contreras Ramos et al. (2018) quantitatively: bulge RRLs have an angular velocity of about $35 \text{ km s}^{-1} \text{ kpc}^{-1}$, i.e., are considerably slower than younger bulge stars ($50\text{--}60 \text{ km s}^{-1} \text{ kpc}^{-1}$). This result is consistent with Wegg et al. (2019), whose sample of halo RRLs rotates with 50 km s^{-1} in their innermost radial bin (1.5 kpc to the Galactic centre). We also find the absence of the velocity dispersion central peak for bulge RRLs with $|b| < 3^\circ$, which is similar to, but more extreme than that for metal-poor RCGs (Ness et al. 2013, their Figure 6).

The halo contamination is not easy to determine, but we offer some clues about the halo/classical bulge fraction (see also Kunder et al. 2016; Pérez-Villegas et al. 2017). We note that Ness et al. (2013) mentioned that the slower rotation in their metal-poor sample may be caused by stars of the metal-weak thick disc and halo which presently lie in the inner Galaxy. This interpretation could also apply to the bulge RRLs. Firstly, the vertical number density of bulge RRLs is distributed exponentially (see Figure 10), not necessarily obeying the stellar-halo-like power law; secondly, we back the claim of Wegg et al. (2019) that the rotation predicted by the Pérez-Villegas et al. (2017) model is too low to be in agreement with the observed rotation from the Gaia DR2 proper motions (see Figure 13), which moderates the claim of Pérez-Villegas et al. (2017) that the RR Lyrae population in the Galactic bulge is consistent with being the inward extension of the Galactic metal-poor stellar halo; thirdly, Savino et al. (2020, a preprint which appeared when our paper was being refereed) analysed the chemodynamical nature of bulge RRLs based on Kunder et al. (2016) data, and found "the

existence of a breaking point in the halo properties at around 5 kpc", which they described as "open to the possibility that the innermost stellar halo is somehow different from its large-scale counterpart".

While the paper was being refereed, a preprint by Kunder et al. (2020) appeared on astro-ph. They presented the results from BRAVA-RR DR2 (cross matched with Gaia DR2), which is a LOS-velocity survey toward RRLs in the Galactic bulge. Their sample size is a factor of 5.9 smaller than ours, but has a substantial advantage since they have 6D phase-space information. They defined "Halo RRL" as the stars with apocenter distances > 3.5 kpc, which composes about 25% of stars in their sample⁵. Since we have not traced the orbits of stars (which is model dependent), we cannot determine this halo fraction precisely. They also found a substantial fraction of "high-velocity stars" ($\sim 7\%$ of stars have 3D velocities greater than 2.5σ from the mean of the distribution); in our sample, the fraction of stars with 2D velocities higher than $2.5\sigma_{2D}=380 \text{ km s}^{-1}$ is about 2%, a factor of 3.5 lower than their fraction. It is unclear whether this can be well explained by the difference between 2D and 3D velocities. Also, their Figure 8 showed that the "Central/Classical RRL" (with $RGC < 0.9$ kpc) have, as mentioned in section 4.4, velocity dispersion similar to younger populations. Furthermore, their sample are non- or slowly rotating (different from "Bar/Bulge RRL"). This is different from the rotation inferred from Gaia proper motions (Figure 11). The difference is likely due to two reasons: 1) our samples are different since they have decontaminated "Halo RRL" (stars with apocenter distances > 3.5 kpc as they defined) while we did not; 2) their sample size is smaller which leads to somewhat larger error bars and make their rotation signal more difficult to see. We are currently studying the issue with radial velocities from APOGEE DR16 to further understand the kinematics of the RRLs in the inner Galaxy. We will present our results in a future paper.

ACKNOWLEDGEMENTS

We thank the referee for insightful comments that improved the paper. We thank István Dékány and Marina Rejkuba for communication on the extinction issue. The research presented here is partially supported by the National Key R&D Program of China under grant No. 2018YFA0404501, by the National Natural Science Foundation of China under grant Nos. 11773052, 11761131016, 11333003, and by a China-Chile joint grant from CASSACA. E.A. thanks the CNES for financial support. This work was granted access to the HPC resources of CINES under the allocations 2018-A0040407665 and 2019-A0040407665 attributed by GENCI (Grand Equipement National de Calcul Intensif). Center de Calcul Intensif Aix-Marseille is acknowledged for granting access to its high-performance computing resources. These two CPU time allocations allowed EA to run and analyze the gas-rich simulation used here. J.S. acknowledges support from a *Newton Advanced Fellowship* awarded by the Royal Society and the Newton Fund. This work made use of the facilities of the Center for High Performance Computing at Shanghai Astronomical Observatory. P.P. has been supported by the National Science Centre, Poland, grant OPUS 2016/23/B/ST9/00655. The original idea was boosted in the 2018 Gaia-LAMOST Sprint workshop, supported by the NSFC under grants 11333003 and 11390372. This work has

⁵ Another recent work (Pietrukowicz et al. 2020), which appeared when our work was being refereed, also concluded that $\sim 25\%$ of the central bulge may be from the halo.

made use of data from the European Space Agency (ESA) mission *Gaia* (<https://www.cosmos.esa.int/gaia>), processed by the *Gaia* Data Processing and Analysis Consortium (DPAC, <https://www.cosmos.esa.int/web/gaia/dpac/consortium>). Funding for the DPAC has been provided by national institutions, in particular the institutions participating in the *Gaia* Multilateral Agreement.

DATA AVAILABILITY

The data generated as part of this project may be shared on a reasonable request to the corresponding author.

REFERENCES

- Alonso-García, J., Dékány, I., Catelan, M., et al. 2015, *AJ*, 149, 99
 Arentsen, A., Starkeburg, E., Martin, N. F., et al. 2020, *MNRAS*, 491, L11
 Athanassoula, E. 1992, *MNRAS*, 259, 328
 Athanassoula, E. & Misiriotis, A. 2002, *MNRAS*, 330, 35
 Athanassoula, E., Rodionov, S. A., & Prantzos, N. 2017, *MNRAS*, 467, L46
 Athanassoula, E., Rodionov, S. A., Pechken, N., et al. 2016, *ApJ*, 821, 90
 Barbuy, B., Chiappini, C., & Gerhard, O. 2018, *ARA&A*, 56, 223
 Binney, J., Gerhard, O., & Spergel, D. 1997, *MNRAS*, 288, 365
 Bissantz, N. & Gerhard, O. 2002, *MNRAS*, 330, 591
 Bland-Hawthorn, J. & Gerhard, O. 2016, *ARA&A*, 54, 529
 Buta, R., Laurikainen, E., Salo, H., et al. 2006, *AJ*, 132, 1859
 Cao, L., Mao, S., Nataf, D., et al. 2013, *MNRAS*, 434, 595
 Cardelli, J. A., Clayton, G. C., & Mathis, J. S. 1989, *ApJ*, 345, 245
 Catelan, M., Pritzl, B. J., & Smith, H. A. 2004, *ApJS*, 154, 633
 Clarke, J. P., Wegg, C., Gerhard, O., et al. 2019, *MNRAS*, 489, 3519
 Clarkson, W., Sahu, K., Anderson, J., et al. 2008, *ApJ*, 684, 1110
 Clarkson, W. I., Calamida, A., Sahu, K. C., et al. 2018, *ApJ*, 858, 46
 Contreras Ramos, R., Minniti, D., Gran, F., et al. 2018, *ApJ*, 863, 79
 Dwek, E., Arendt, R. G., Hauser, M. G., et al. 1995, *ApJ*, 445, 716
 Dékány, I., Minniti, D., Catelan, M., et al. 2013, *ApJ*, 776, L19
 Dékány, I., Hajdu, G., Grebel, E. K., et al. 2019, *ApJ*, 883, 58
 Dékány, I., Hajdu, G., Grebel, E. K., et al. 2018, *ApJ*, 857, 54
 Eilers, A.-C., Hogg, D. W., Rix, H.-W., et al. 2019, *ApJ*, 871, 120
 Elorrieta, F., Eyheramendy, S., Jordán, A., et al. 2016, *A&A*, 595, A82
 Freeman, K., Ness, M., Wylie-de-Boer, E., et al. 2013, *MNRAS*, 428, 3660
 Fux, R. 1999, *A&A*, 345, 787
 Gaia Collaboration, Katz, D., Antoja, T., et al. 2018, *A&A*, 616, A11
 Gaia Collaboration, Prusti, T., de Bruijne, J. H. J., et al. 2016, *A&A*, 595, A1
 Gonzalez, O. A., Rejkuba, M., Zoccali, M., et al. 2012, *A&A*, 543, A13
 Gonzalez, O. A., Rejkuba, M., Zoccali, M., et al. 2011, *A&A*, 534, A3
 Grady, J., Belokurov, V., & Evans, N. W. 2020, *MNRAS*, 492, 3128
 Gran, F., Minniti, D., Saito, R. K., et al. 2016, *A&A*, 591, A145
 Gravity Collaboration, Abuter, R., Amorim, A., et al. 2019, *A&A*, 625, L10
 Hajdu, G., Dékány, I., Catelan, M., et al. 2020, *Experimental Astronomy*, 49, 217
 Howard, C. D., Rich, R. M., Reitzel, D. B., et al. 2008, *ApJ*, 688, 1060
 Kunder, A., Pérez-Villegas, A., Rich, R. M., et al. 2020, *AJ*, 159, 270
 Kunder, A., Koch, A., Rich, R. M., et al. 2012, *AJ*, 143, 57
 Kunder, A., Rich, R. M., Koch, A., et al. 2016, *ApJ*, 821, L25
 Li, Z.-Y. & Shen, J. 2012, *ApJ*, 757, L7
 Lindegren, L., Hernández, J., Bombrun, A., et al. 2018, *A&A*, 616, A2
 López-Corredoira, M., Cabrera-Lavers, A., & Gerhard, O. E. 2005, *A&A*, 439, 107
 Marconi, M., Coppola, G., Bono, G., et al. 2015, *ApJ*, 808, 50
 Mateu, C. & Vivas, A. K. 2018, *MNRAS*, 479, 211
 Minniti, D., Lucas, P. W., Emerson, J. P., et al. 2010, *New Astron.*, 15, 433
 Minniti, D., Dékány, I., Majaess, D., et al. 2017, *AJ*, 153, 179
 Nataf, D. M., Gould, A., Fouqué, P., et al. 2013, *ApJ*, 769, 88
 Ness, M., Freeman, K., Athanassoula, E., et al. 2013, *MNRAS*, 432, 2092
 Ness, M., Freeman, K., Athanassoula, E., et al. 2013, *MNRAS*, 430, 836

- Ness, M., Zasowski, G., Johnson, J. A., et al. 2016, *ApJ*, 819, 2
- Peschken, N., Athanassoula, E., & Rodionov, S. A. 2017, *MNRAS*, 468, 994
- Pietrukowicz, P., Udalski, A., Soszyński, I., et al. 2020, arXiv:2007.05849
- Pietrukowicz, P., Udalski, A., Soszyński, I., et al. 2012, *ApJ*, 750, 169
- Pietrukowicz, P., Kozłowski, S., Skowron, J., et al. 2015, *ApJ*, 811, 113
- Pérez-Villegas, A., Portail, M., & Gerhard, O. 2017, *MNRAS*, 464, L80
- Qin, Y., Shen, J., Li, Z.-Y., et al. 2015, *ApJ*, 808, 75
- Rattenbury, N. J., Mao, S., Sumi, T., et al. 2007, *MNRAS*, 378, 1064
- Reid, M. J. & Brunthaler, A. 2004, *ApJ*, 616, 872
- Rojas-Arriagada, A., Recio-Blanco, A., Hill, V., et al. 2014, *A&A*, 569, A103
- Rojas-Arriagada, A., Recio-Blanco, A., de Laverny, P., et al. 2017, *A&A*, 601, A140
- Sanders, J. L., Smith, L., Evans, N. W., et al. 2019, *MNRAS*, 487, 5188
- Savino, A., Koch, A., Prudil, Z., et al. 2020, arXiv:2006.12507
- Shen, J., Rich, R. M., Kormendy, J., et al. 2010, *ApJ*, 720, L72
- Simion, I. T., Belokurov, V., Irwin, M., et al. 2017, *MNRAS*, 471, 4323
- Smolec, R. 2005, *Acta Astron.*, 55, 59
- Soszyński, I., Udalski, A., Szymański, M. K., et al. 2014, *Acta Astron.*, 64, 177
- Soszyński, I., Udalski, A., Wrona, M., et al. 2019, *Acta Astron.*, 69, 321
- Stanek, K. Z., Udalski, A., Szymański, M., et al. 1997, *ApJ*, 477, 163
- Surot, F., Valenti, E., Hidalgo, S. L., et al. 2019, *A&A*, 629, A1
- Udalski, A., Szymański, M. K., & Szymański, G. 2015, *Acta Astron.*, 65, 1
- Walker, A. R. 1989, *PASP*, 101, 570
- Wegg, C. & Gerhard, O. 2013, *MNRAS*, 435, 1874
- Wegg, C., Gerhard, O., & Bieth, M. 2019, *MNRAS*, 485, 3296
- Zasowski, G., Ness, M. K., García Pérez, A. E., et al. 2016, *ApJ*, 832, 132
- Zoccali, M., Vasquez, S., Gonzalez, O. A., et al. 2017, *A&A*, 599, A12